Applied Surface Science 697 (2025) 163015

Contents lists available at ScienceDirect

Applied Surface Science

journal homepage: www.elsevier.com/locate/apsusc

Full Length Article

Enhanced hydrogen evolution ability of Ru with regulation of interface electronic structure by WC/W_2C heterostructure via ultrafast flash joule heating synthesis

Yongkang Liu [a], Fulai Qi [a,*], Xinqiang Wang [a], Qian Zhang [a], Yanxia Liu [a], Yong Gao [a], Ke Wang [a], Wengang Cui [a], Fan Gao [a], Zhenglong Li [a], Yaxiong Yang [a], Lixian Sun [b], Jian Chen [a], Hongge Pan [a,*]

[a] Institute of Science and Technology for New Energy Xi'an Technological University, Xi'an 710021, PR China
[b] School of Material Science & Engineering, Guangxi Key Laboratory of Information Materials and Guangxi, Collaborative Innovation Center of Structure and Property for New Energy and Materials, Guilin University of Electronic Technology, Guilin 541004, PR China

ARTICLE INFO

Keywords:
Ruthenium
Tungsten carbide
Heterointerface
Hydrogen evolution reaction
Proton exchange membrane water electrolysis

ABSTRACT

Regulation of the electronic structure for ruthenium (Ru) based catalysts is critical but challenging to achieve highly active and stable performance at ampere-level current density for proton exchange membrane water electrolysis (PEMWE). In this work, two phase tungsten carbide heterostructure interface (WC/W_2C) is constructed to optimize adsorption of hydrogen intermediates (H*) on Ru-based heterostructure catalyst by one-step ultrafast flash joule heating. Experimental and theoretical studies indicate the obvious charge accumulation and migration at the interface region between Ru and WC/W_2C heterostructure. The H* adsorption and desorption balanced by tuning the interface electronic structure contributes synergistic effect to the HER activity of Ru-W_xC/CC. Accordingly, with a trace amount of Ru, the as-synthesized Ru-W_xC/CC exhibits an overpotential of 31 mV at 10 mA cm^{-2} and 288 mV at 1 A cm^{-2}. Furthermore, the catalyst delivers exceptional stability during at least 500 h of operation at 10 mA cm^{-2} with negligible degradation for overall water splitting. This work will provide a guidance for regulating interfacial electronic structure of hydrogen evolution catalyst by the design of heterostructure.

1. Introduction

Proton exchange membrane water electrolysis (PEMWE) can produce large-scale green hydrogen from renewable energy [1–4], due to its high energy efficiency, substantial current density, swift response time, and exceptional gas purity [5–8]. Where the highly efficient, low-cost, and stable catalysts for hydrogen evolution reaction (HER) play a significant role in promoting the performance of PEMWE devices. Platinum (Pt) is recognized as the state-of-the-art electrocatalyst toward HER, but its high cost and low reserves directly limit the large-scale application of PEMWE [9–13]. Over the past few decades, the catalytic activity of non-noble metal catalysts has significantly increased but is still not comparable with Pt/C due to their low intrinsic catalytic induced by the electronic structures [14–16].

Ruthenium (Ru), a relatively low-priced platinum-group metal with Pt-like metallic-H bond strength (65 kcal mol^{-1}), has garnered considerable attention as a promising alternative [17–20]. Although Ru has potentially high HER activity, it is prone to agglomerate due to its larger cohesion energy than Pt [21]. Recent studies have designed uniform dispersion of Ru nanoparticles (NPs) [22], nanoclusters [23] and single-atom [24,25] catalysts. Uniformly dispersed Ru sites allow maximum utilization of metal species and increase efficiency. Additionally, the interaction between Ru and substrate has been proved to be crucial to regulate the surface physicochemical properties and electronic structure of Ru-based catalysts. The distinct hetero-interfacial effects occurring in the heterostructures can guide electronic reconstruction, binding energy optimization, active site enlargement, and electron transfer acceleration [26–28].

Metallic Ru-based heterostructure catalysts have attracted much attention in the field of electrocatalysis due to their excellent properties and the modification of electronic states at the heterogeneous interface [24]. Ren et al. designed Ru nanoclusters on carbon supports doped with

* Corresponding authors.
E-mail addresses: qifulai@xatu.edu.cn (F. Qi), hgpan@zju.edu.cn, honggepan@zju.edu.cn (H. Pan).

https://doi.org/10.1016/j.apsusc.2025.163015
Received 4 January 2025; Received in revised form 20 February 2025; Accepted 17 March 2025
Available online 18 March 2025

controllable N-functional groups (NDC) carriers. The accumulation of electrons at the interface between the NDC carrier and Ru nanoclusters led to the asymmetric distribution of electrons, which promoted the adsorption and dissociation of water around the Ru sites [29]. In addition to the construction of heterogeneous structures with non-metallic carriers and single metallic Ru, there are also many studies on metal carbides/phosphates/sulfides/nitrides [30,31]. Metal carbides are widely used because of their excellent chemical and thermal stability, excellent corrosion resistance, and high electrical conductivity [32,33]. Specifically, metal carbide carriers promote the dispersion of metal atoms through strong electron interactions, triggering orbital hybridization and charge polarization at the interface to regulate catalytic activity [34,35]. In addition, metal carbide carriers combined with the potent H* binding energy of Ru NPs will enhance the catalytic activity of HER significantly [36]. Li et al. constructed a β-Mo_2C-Ru nanoparticle heterogeneous catalyst. The interfacial interaction and strong electron coupling between Ru and Mo_2C optimized the adsorption/desorption of hydrogen intermediates and accelerated the acidic HER kinetics [37]. Jiang et al. realized efficient interfacial charge transfer by constructing lattice-matched Ru/W_2C heterogeneous interfaces. The H* adsorbed on the surface of W_2C rapidly migrated to the Ru site through the heterogeneous interface to reduce the hydrolytic dissociation barrier. Ru as a highly efficient H* desorption site accelerated H-H coupling [38]. In summary, the activity of metallic Ru-based heterostructure catalysts is strongly dependent on a rich and highly active interface [24]. The two-phase heterostructure restricts the flexibility of adjustable characteristics of heterointerface. Accordingly, the design and construction of multi-phase heterostructure catalysts can open an avenue toward efficient heterostructure catalysts.

Herein, we constructed a Ru-based heterostructure catalyst by ultrafast flash joule heating. Ru NPs are uniformly dispersed on the heterostructure of WC/W_2C. With a trace amount of Ru, the as-synthesized Ru-W_xC/CC exhibits an overpotential of 31 mV at 10 mA cm^{-2} and 288 mV at 1 A cm^{-2}. Density functional theory reveals the obvious charge accumulation and migration at the interface region of Ru-WC/W_2C heterostructure. The partial electrons transfer from Ru NPs to W_xC. The weakening of Ru-H bond promotes the desorption of H intermediate on Ru active sites. The ΔG_{H^*} of Ru-W_xC/CC approaches to 0 eV, which can optimize hydrogen adsorption/desorption strength significantly and reduce HER reaction energy barrier. Furthermore, the catalyst delivers exceptional stability during at least 500 h of operation at 10 mA cm^{-2} with negligible degradation for overall water splitting.

2. Experimental section

Detailed information was given in Supplementary Materials.

3. Results and discussion

3.1. Synthesis and characterizations of electrodes

In this work, the ultrafast flash joule heating technology was employed. Compared with traditional technology, this method can synthesize uniformly dispersed materials with remarkable steadiness swiftly in a short time. The structure and morphology of the catalyst can be controlled by changing the joule heating conditions [39–43]. Fig. 1a displayed the synthesis procedure of the Ru-W_xC/CC. Primarily, the carbon cloth (CC) substrate was treated in 65 % HNO_3 solution to increase surface hydrophilicity. Subsequently, the treated CC was immersed into 2 % polyethylenimide (PEI) solution to modulate the surface state of charge. PEI, characterized as a high C and N polymer, can shift the CC surface from negative charge state to positive charge

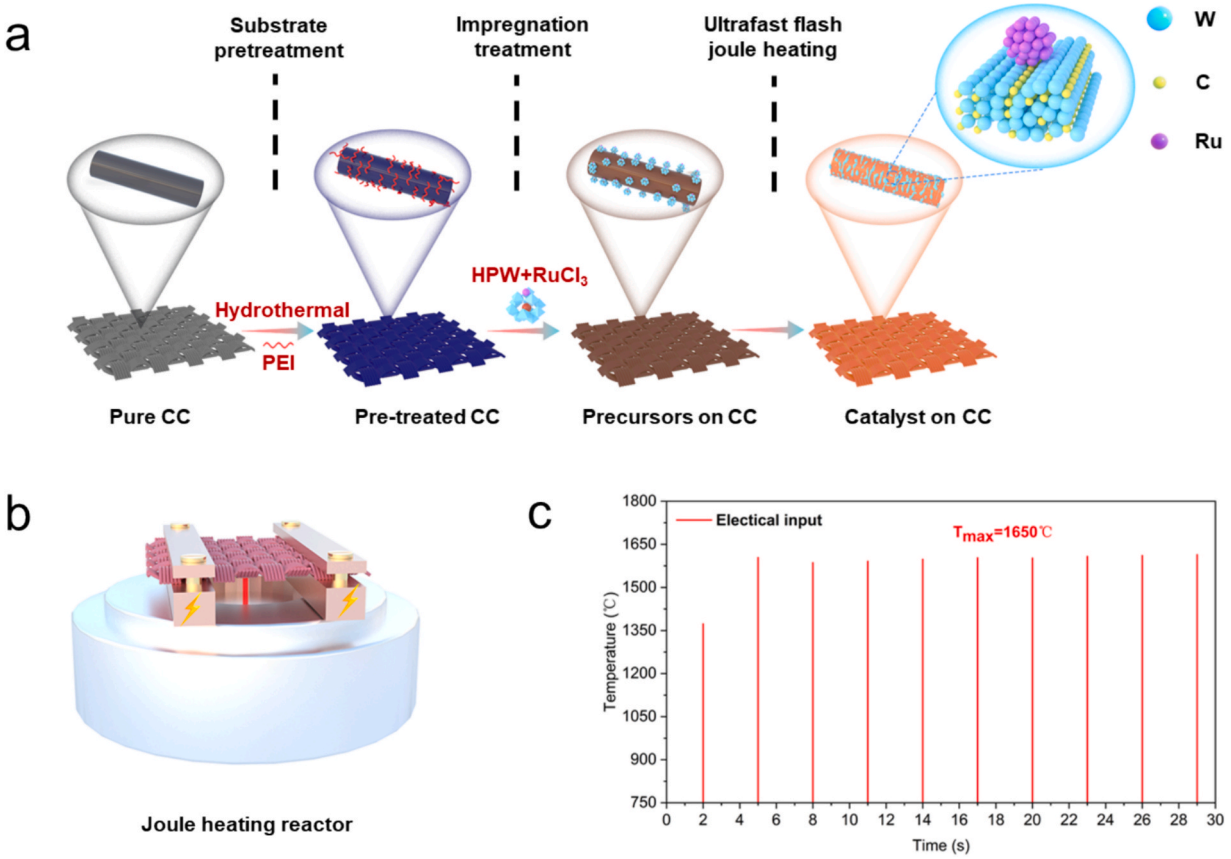

Fig. 1. a) Schematic illustration of the synthesis of Ru-W_xC/CC by the ultrafast flash joule heating synthesis. b) Schematic diagram of the working condition of the joule heating reactor. c) A ten-pulse shock heating pattern demonstrates the uniform temperature in each cycle.

state [44,45]. For improving the dispersion of Ru NPs, the phosphotungstic acid anion (PW_{12}^{3-}) was chosen to adsorb and stabilize Ru^{3+} cations. The CC was impregnated into an ethanol solution containing PW_{12}^{3-}/Ru^{3+} clusters. The PW_{12}^{3-}/Ru^{3+} clusters with negative charge could be adsorbed on CC surface with positive charge [46,47]. Ultimately, the dry CC was rapidly heated to 1650 °C for 100 ms by ultrafast flash joule heating in a vacuum atmosphere. Fig. 1b displayed the joule heating reaction device. In detail, two copper plates are used to fix the CC to form a conductive channel. The current flows through the CC via the conductive copper plate with a certain applied voltage. Due to joule heating effect, the CC carrier reaches the target temperature in a short time. Fig. 1c showed the temperature distribution during 10 joule heating pulse with 100 ms heating time. During calcination, the temperature was very stable. PW_{12}^{3-} was instantaneously pyrolyzed to form W_xC, and Ru^{3+} was reduced to metallic Ru [41,48,49]. Due to the preformed PW_{12}^{3-}/Ru^{3+} cluster structure, the Ru NPs were uniformly dispersed and directly combined with the W_xC carrier to form heterostructures.

The scanning electron microscopy (SEM) images of the Ru-W_xC/CC, Ru/CC and W_xC/CC were shown in Fig. 2a–b and Fig. S1. The Ru-W_xC/CC exhibited the uniform nanoislands shape on the carbon fiber. The Ru/CC showed different morphology, and the spherical nanoparticles were distributed on the surface of the carbon fiber. The SEM images of the catalysts obtained with varying amounts of Ru and phosphotungstic acid (HPW) were shown in Figs. S2-3. The morphology of catalyst did not change too much with the loading of Ru and HPW. The SEM images of the catalysts obtained with varying amounts of the joule heating time and temperatures were shown in Figs. S4-5. With the increase of joule heating time, the size of catalyst increased obviously and the particles were agglomerated together. With the temperature increased, the particle size of the catalyst gradually became bigger. And at 1850 °C, most of the particles were aggregated on the surface of the CC, which limited the mass transfer during the catalytic process and thus reduced the catalytic activity. The TEM of Ru-W_xC/CC and W_xC/CC at different resolutions were shown in Fig. 2c and Figs. S6-7. The high-resolution transmission electron microscopy (HRTEM) images confirmed the presence of Ru, WC, and W_2C three phases in Fig. 2d. The observed d-spacings of 0.173 nm, 0.259 nm, 0.203 nm corresponded to the (102) of W_2C, (100) of WC, and (002) of Ru, separately. The selected area electron diffraction (SAED) pattern showed the diffraction patterns indexed to the (100) plane of WC, (102) plane of W_2C and (002) plane of Ru in Fig. 2e. The elemental mapping in Fig. 2f demonstrated that the Ru-W_xC/CC was mainly composed of W, C and O elements, as well as a small amount of Ru (Fig. S8). Therefore, three-phase heterostructures were successfully constructed. For the W_xC/CC in Fig. S9, the observed d-spacings of 0.250 nm, 0.172 nm corresponded to the (100) of WC and the (102) of W_2C, separately. The SAED pattern showed the diffraction patterns were indexed to the (100), (011) plane of WC and (002), (102) plane of W_2C. The element mapping diagram of the W_xC/CC revealed the uniform distribution of W, O and C. ICP-MS was used to precisely quantitate the metal element amounts in Ru-W_xC/CC, as depicted in Table S1. The content of Ru was merely 1.44 wt%.

X-ray diffraction (XRD) was used to further confirm the crystal structure of the as-synthesized Ru-W_xC/CC, Ru/CC, W_xC/CC and CC (Fig. 3a). In the Ru-W_xC/CC, the characteristic peaks at 31.51°, 35.64° and 48.29° are assigned to the (001), (100) and (101) planes of WC phase, the characteristic peaks at 34.53°, 39.59° and 43.23° are assigned to the (110), (−1–11) and (102) planes of W_2C phase. This suggested the presence of two-phase W_xC NPs within the catalyst. The presence of three Ru diffraction peaks at 37.73°, 42.17° and 43.43° are assigned to the (100), (002) and (101) planes. The diffraction peaks of Ru were relatively weak, because of its ultralow content and well-distribution. This was consistent with the ICP-MS result. Similarly, the XRD result also proved that three-phase heterostructures were successfully constructed. Compared with W_xC/CC, introducing Ru into W_xC resulted in the diffraction peak intensity of Ru and W_xC diminished, and the phase content of WC/W_2C phases changed. These findings aligned with those derived from both SEM and TEM characterization. Figs. S10-11 displayed the XRD results of catalysts with different concentrations of Ru and HPW. It was found that the position of the diffraction peak remained constant.

Raman spectrum was utilized to delve deeper into the structural details of Ru-W_xC/CC, W_xC/CC, and Ru/CC. In Fig. 3b, the peaks at 698 cm^{-1} and 861 cm^{-1} could be attributed to the W-C stretching mode, implying the formation of the W_xC phase [50]. The presence of a particular peak at 625 cm^{-1} might be related to the introduction of Ru, but the peak was very weak, possibly due to the minimal presence of Ru, indicating that Ru NPs were successfully introduced. In Fig. S12, D-band

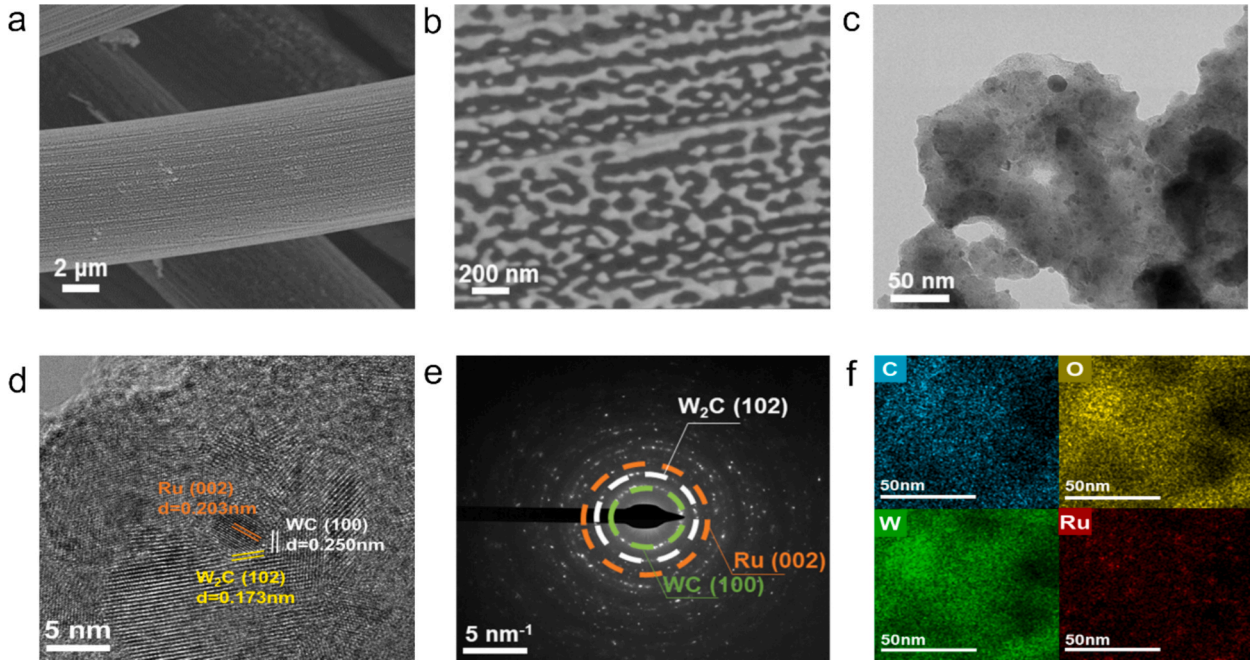

Fig. 2. a) and b) SEM images at different resolutions, c) TEM image, d) HRTEM image, e) SAED pattern f) EDS mapping diagram of Ru-W_xC/CC.

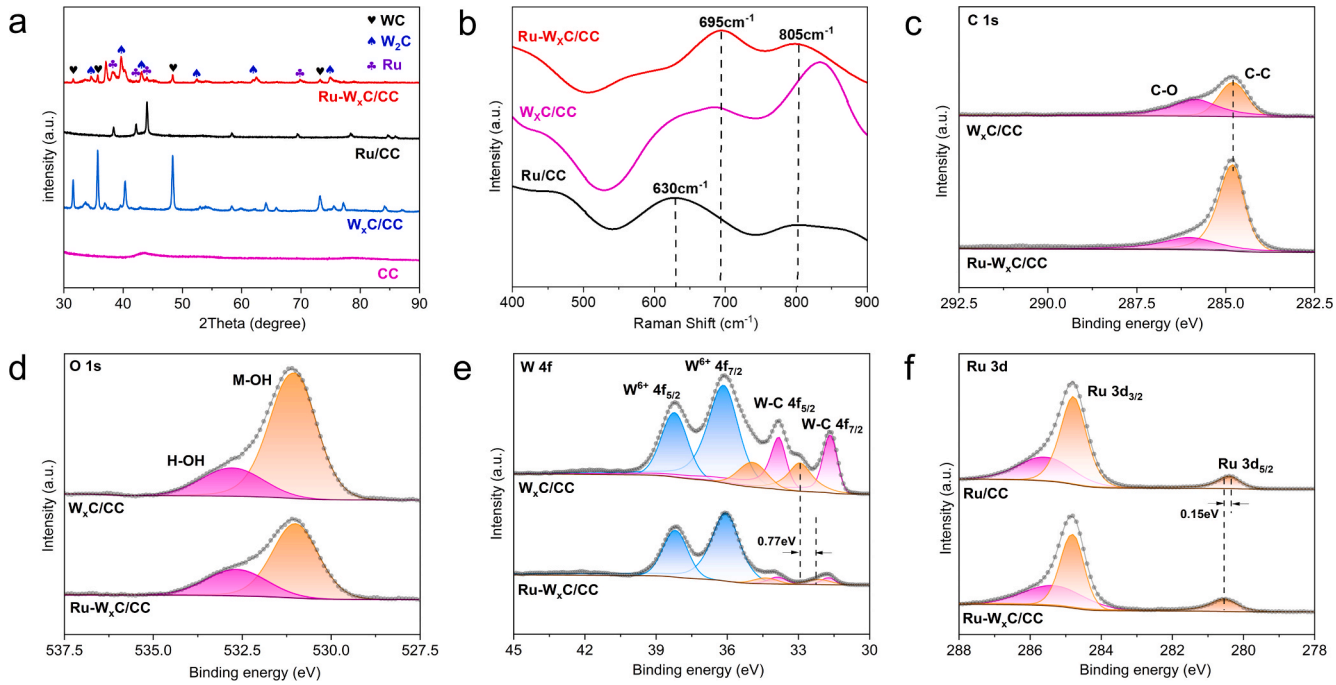

Fig. 3. a) XRD and b) Raman spectrum of ru-w$_x$C/CC, W$_x$C/CC, and Ru/CC. c) C 1 s, d) O 1 s, e) W 4f and f) Ru 3d XPS spectra of Ru-W$_x$C/CC and W$_x$C/CC.

peak at 1350 cm^{-1} corresponding to defective carbon and G-band peak at 1600 cm^{-1} corresponding to graphitized carbon appeared. The I_G:I_D value of Ru-W$_x$C/CC was higher, indicating that Ru-W$_x$C/CC had higher conductivity, which was conducive to HER electrocatalytic hydrogen extraction performance [51,52].

X-ray photoelectron spectroscopy (XPS) was employed to gain a profound understanding of the valence state and distinctive electronic structure of the pristine Ru-W$_x$C/CC. The Ru, W, C and O elements could be clearly observed in the full-scan XPS survey spectrum of Ru-W$_x$C/CC (Fig. S13). There was no obvious signal of P and Cl elements in Ru-W$_x$C/CC, which was ascribed to the vaporization of the elements at high temperature. In the C 1 s spectrum (Fig. 3c), the peaks at binding energy of 284.80 eV and 286.06 eV are assigned to C—C and C—O, respectively. Two characteristic peaks, namely hydroxyl group adsorbed on the surface of mental element (M—OH) (531.01 eV) and oxygen from adsorbed water (H—OH) (532.66 eV) on the surface of the material, could be observed in O 1 s spectrum (Fig. 3d) [53]. The W 4f spectrum of Ru-W$_x$C/CC (Fig. 3e) could be deconvoluted into three pairs of characteristic peaks. Two strong peaks at binding energy of 36.06 eV and 38.19 eV are assigned to the W^{6+} $4f_{7/2}$ and W^{6+} $4f_{5/2}$ orbitals, respectively. Two strong peaks at binding energy of 31.71 eV and 33.88 eV are assigned to the W-C $4f_{7/2}$ and W-C $4f_{5/2}$ orbitals, respectively. They corresponded to W^{2+} valence states. Two satellite peaks at binding energy of 32.16 eV and 34.38 eV corresponded to W^{4+} valence states [54]. The presence of W^{6+} might stem from surface oxidization, which in turn enhanced the W^{4+} valence. Compared with W$_x$C/CC, the lower proportion for high valence W^{6+} peak in Ru-W$_x$C/CC indicated that the surface oxidation degree of Ru-W$_x$C/CC was lower than that of W$_x$C/CC [55]. The ratio of W^{4+} and W^{2+} peak areas in Ru-W$_x$C/CC was approximately 1:1, indicating the presence of a mixture of WC and W_2C phases. However, the signal intensity and ratio of W^{4+} and W^{2+} in W$_x$C/CC were significantly stronger than that in Ru-W$_x$C/CC. The content of high valence W^{4+} might adsorb hydrogen intermediate (H*) through stronger W-H bond in HER reaction, but too strong adsorption could lead to desorption difficulty and inhibit HER kinetics [56,57]. Proper ratio of W^{4+} to W^{2+} could optimize the adsorption/desorption equilibrium of H* and increase the activity of HER. The binding energy of W^{4+} within Ru-W$_x$C/CC negatively shifted to lower binding energy compared with W$_x$C/CC which indicated electrons were transferred between W_2C and WC. This proved that abundant electron transfer from W_2C to WC through two-phase interface. In the Ru 3d spectrum of Ru-W$_x$C/CC (Fig. 3f), the peaks at binding energy of 284.79 eV and 280.55 eV are assigned to Ru $3d_{3/2}$ and Ru $3d_{5/2}$ of metallic Ru, respectively, and the one weak peak at binding energy of 285.4 eV is assigned to oxidized Ru species [4]. The binding energy of metallic Ru^0 species gradually moved to the higher binding energy direction relative to the Ru/CC contrast sample, indicating that the introduction of Ru led to partial electrons transport from Ru NPs to W$_x$C. The above XPS results demonstrated that there was charge transfer between Ru and W$_x$C, and strong electronic coupling around the three-phase heterogeneous interface, which could effectively regulate the electronic structure of Ru.

3.2. Electrochemical measurement of HER activities

The HER activity of Ru-W$_x$C/CC, W$_x$C/CC, Ru/CC and commercial Pt/C were evaluated in 0.5 M H_2SO_4 using a three-electrode system. The content of Ru and HPW were optimized, as shown in Fig. S14-15. When the mas loading of Ru and HPW were 0.56 mg cm^{-2} and 4 mg cm^{-2} respectively, the catalyst possessed optimal HER activity. In Fig. 4a, the LSV polarization curve showed that the overpotential of Ru-W$_x$C/CC was 31 mV at 10 mA cm^{-2} current density. The activity was comparable to that of the commercially available 20 % Pt/C catalyst (0.5 mg cm^{-2} loading). For comparison, the W$_x$C/CC delivered an overpotential of 218 mV and Ru/CC with the identical Ru loading had an overpotential of 67 mV, which illustrated that Ru site was dominated in the HER activity and required to be regulated. Additionally, Ru-W$_x$C/CC enabled to operate at 1 A cm^{-2} current density with an overpotential of 288 mV. The activity enhancement of Ru-W$_x$C/CC was mainly derived from the regulation effect of WC/W_2C heterostructures on Ru electronic structure.

The Tafel curves were fitted from the LSV curve to distinguish the HER mechanism in Fig. 4b. For the W$_x$C/CC, the Tafel slope reached 70 mV/dec, indicating that the Volmer step of proton adsorption on the catalyst surface was the Rate-Determining Step (RDS). After the integration of Ru, the Tafel slope dropped to 43.15 mV dec^{-1}, which was close to the theoretical value of the Heyrovsky step (40 mV dec^{-1}),

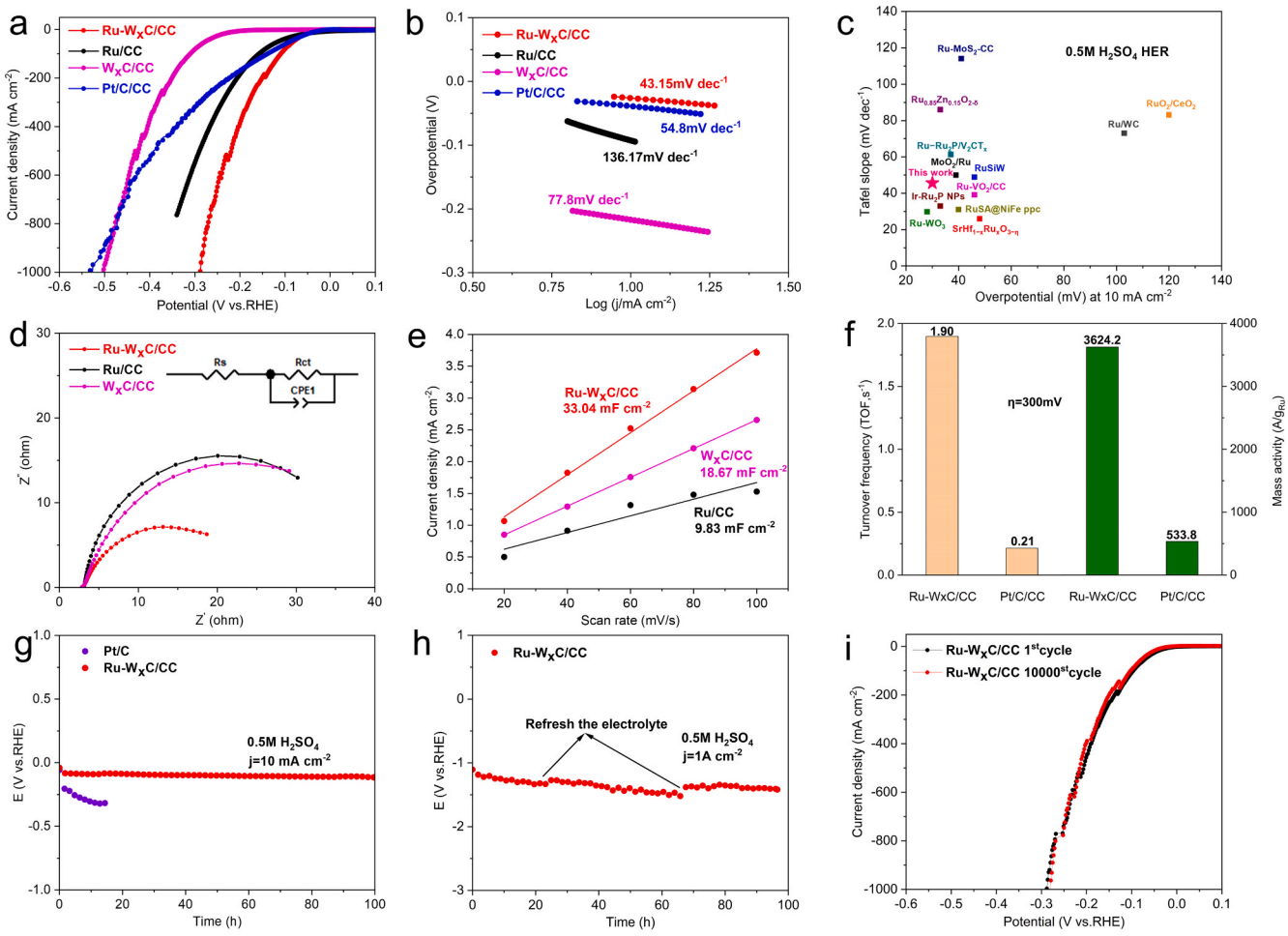

Fig. 4. a) LSV curves of Ru-W_xC/CC, Ru/CC, W_xC/CC and 20 % Pt/C/CC in 0.5 M H_2SO_4. b) Tafel curves of Ru-W_xC/CC, Ru/CC, W_xC/CC in 0.5 M H_2SO_4. c) Comparison of the activity of Ru-based hydrogen evolution catalysts. d) EIS curves, e) C_{dl} curves of Ru-W_xC/CC, Ru/CC, W_xC/CC. f) Comparison of TOF and Mass activity values of Ru-W_xC/CC and 20 % Pt/C/CC when η = 300 mV. g) Stability comparison at 10 mA cm^{-2} of Ru-W_xC/CC and 20 % Pt/C/CC. h) Stability of Ru-W_xC/CC at 1 A cm^{-2}. i) Ru-W_xC/CC acceleration stress curve.

indicating more rapid HER kinetics. The HER occurred via the Volmer-Heyrovsky mechanism. The overpotential and Tafel slope of the Ru-W_xC/CC at 10 mA cm^{-2} were compared with the reported Ru-based hydrogen evolution catalysts (Fig. 4c), and the results showed that the kinetics were better than most reported catalysts. The decreased slope suggested that the adsorption/desorption strength of H intermediates on the Ru-W_xC/CC had been optimized via a synergistic effect between Ru and WC/W_2C heterostructures.

Electrochemical impedance spectroscopy (EIS) measurements were conducted to profoundly investigate the outstanding HER activities of the Ru-W_xC/CC. The fitted Nyquist plots in Fig. 4d showed the charge transfer resistance of Ru-W_xC/CC (10.3 Ω) is much lower than that of W_xC/CC (20 Ω) and Ru/CC (17.2 Ω) in 0.5 M H_2SO_4 solution, confirming that the catalyst exhibited fast electron transfer capability toward the HER.

The specific surface area of the electrochemical activity of catalysts is one of the important factors to affect the catalytic activity of catalysts. The cyclic voltammetry (CV) curve of the catalysts in the non-Faraday region was measured in 0.5 M H_2SO_4 solution by different scan rates. The CV curves with different Ru and HPW contents were shown in Fig. S16-17. The CV curve was fitted to obtain the correlation curve with current density at different sweeping rates, and the slope was calculated to obtain the capacitance value of the electrochemical double-layer capacitance (C_{dl}) (Fig. 4e). The Ru-W_xC/CC had a higher double layer capacitance of 33.04 mF cm^{-2}, while W_xC/CC and Ru/CC had a double layer capacitance of 18.67 mF cm^{-2} and 9.83 mF cm^{-2}, respectively. The C_{dl} with different Ru and HPW contents were shown in Fig. S18. The electrochemical surface area (ECSA) was normalized from LSV curves (Fig. S19). The ECSA of Ru-W_xC/CC was 944 cm^2 which was much higher than that of W_xC/CC, which illustrated that Ru-W_xC/CC exhibited the higher intrinsic activity than W_xC/CC. Therefore, the HER activity of the catalyst was essentially enhanced.

The Ru clusters in Ru-W_xC/CC with high surface-to-volume provided highly exposed active sites to significantly improve the metal utilization efficiency of Ru. As shown in Fig. 4f. When the overpotential was 300 mV, the mass activity of the catalyst was 3624.2 A g^{-1} and the TOF value was 1.9 s^{-1}, surpassing commercial Pt/C by 6.8- and 9- fold, respectively.

The long-term stability of the Ru-W_xC/CC was further estimated by chronopotentiometry (CP) test in 0.5 M H_2SO_4 solution. In Fig. 4g, the Ru-W_xC/CC exhibited long-term stability for over 100 h at 10 mA cm^{-2}, whereas Pt/C only operated 10 h. The Ru-W_xC/CC also operated stably for more than 100 h at 500 mA cm^{-2} and 1A cm^{-2} in Fig. 4h and Fig. S20. The overpotential decayed at the rate of 0.3 mV/h. In parallel, the polarization curve of Ru-W_xC/CC (Fig. 4i) exhibited insignificant performance deterioration. The overpotential declined about 5 mV at 10 mA cm^{-2} after 10,000 continuous CV cycles at the scan rate of 100 mV/s, suggesting its satisfactory durability under acidic condition. Subsequently, we analyzed the crystal structure before and after HER by XRD in Fig. S21. The XRD pattern showed that the position of the peak

did not change after the XRD test, indicating that the crystal structure after HER remained intact. We also analyzed the chemical states of C, O, Ru, and W in Ru-W_xC/CC after HER by XPS in Fig. S22. The C 1 s spectrum showed that C occurred a certain degree of oxidation. The O 1 s spectrum showed that the content of oxygen from adsorbed water is significantly increased. The Ru 3d spectrum showed that the metallic Ru^0 disappeared near 280 cm^{-1}, indicating a slight dissolution of Ru species. The W 4f spectrum after the test showed that the low state peak of W disappeared, which proved that W occurred a slight oxidation.

The overall water splitting was evaluated in 0.5 M H_2SO_4 by directly using Ru-W_xC/CC as cathode and $RuWO_x$/CC as anode in Fig. 5a. The preparation of $RuWO_x$/CC was indicated in the experimental details. In contrast to the preparation of Ru, it was sintered directly in the air. As a comparison, 20 % Pt/C and $RuWO_x$/CC were adopted as cathode and anode, respectively. In Fig. 5b, the Ru-W_xC/CC || $RuWO_x$/CC cell showed a cell voltage of 2.09 V @1000 mA cm^{-2} which was higher than the Pt/C || $RuWO_x$/CC cell. As shown in Fig. 5c, The Ru-W_xC/CC || $RuWO_x$/CC cell showed higher stability. After CP tested up to at least 500 h @10 mA cm^{-2}, the voltage of Ru-W_xC/CC || $RuWO_x$/CC cell had only 100 mV voltage increase. The voltage maintained the initial values of 99.3 % after 500 h operation. While the Pt/C || $RuWO_x$/CC cell only operated for 275 h before it completely lost its full activity. Therefore, The Ru-W_xC/CC was suitable for commercial use and meets the requirements of actual working conditions because of its excellent overall water splitting activity.

3.3. Mechanism for the enhancement of HER in acid

To further reveal the adsorption behavior of hydrogen on the catalyst surface during HER, in-situ Raman spectrum were conducted in acidic media (Fig. S23). The voltage range was selected from −0.4~0.2 V (relative to the reversible hydrogen electrode (RHE)), including the non-Faraday region and HER hydrogen evolution region. At a specific potential of 0.1 V (vs. RHE), the surface of catalyst began to adsorb the hydrogen protons. A new peak appeared near 2325 cm^{-1}, which might be attributed to the result of Ru-H stretching vibration. The intensity of this peak further rose with increasing the applied cathodic potential. In this process, the rate-determining step (RDS) changed from the Volmer step to the Heyrovsky or Tafel step. Therefore, the H on Ru was a reaction intermediate in the HER, and the Ru-H bond was an important factor in determining HER activity [58,59]. Similarly, in infrared spectrum (Fig. S24), there was no significant change before impregnation. After impregnation, the absorption peak in the range of 600~1000 cm^{-1} associated with W-O stretching modes. After carbonization, the absorption peak in the range of 600~800 cm^{-1} associated with W-C stretching modes. After the HER hydrogen evolution test, the peaks in the range of 1500~2000 cm^{-1} related to the formation of the Ru-H bond, whereas the peaks near 1200 cm^{-1} associated with the formation of the W-H bond. The above results showed that W and Ru were bonded to H during the HER process.

The superior catalytic performance of the Ru-W_xC/CC was further

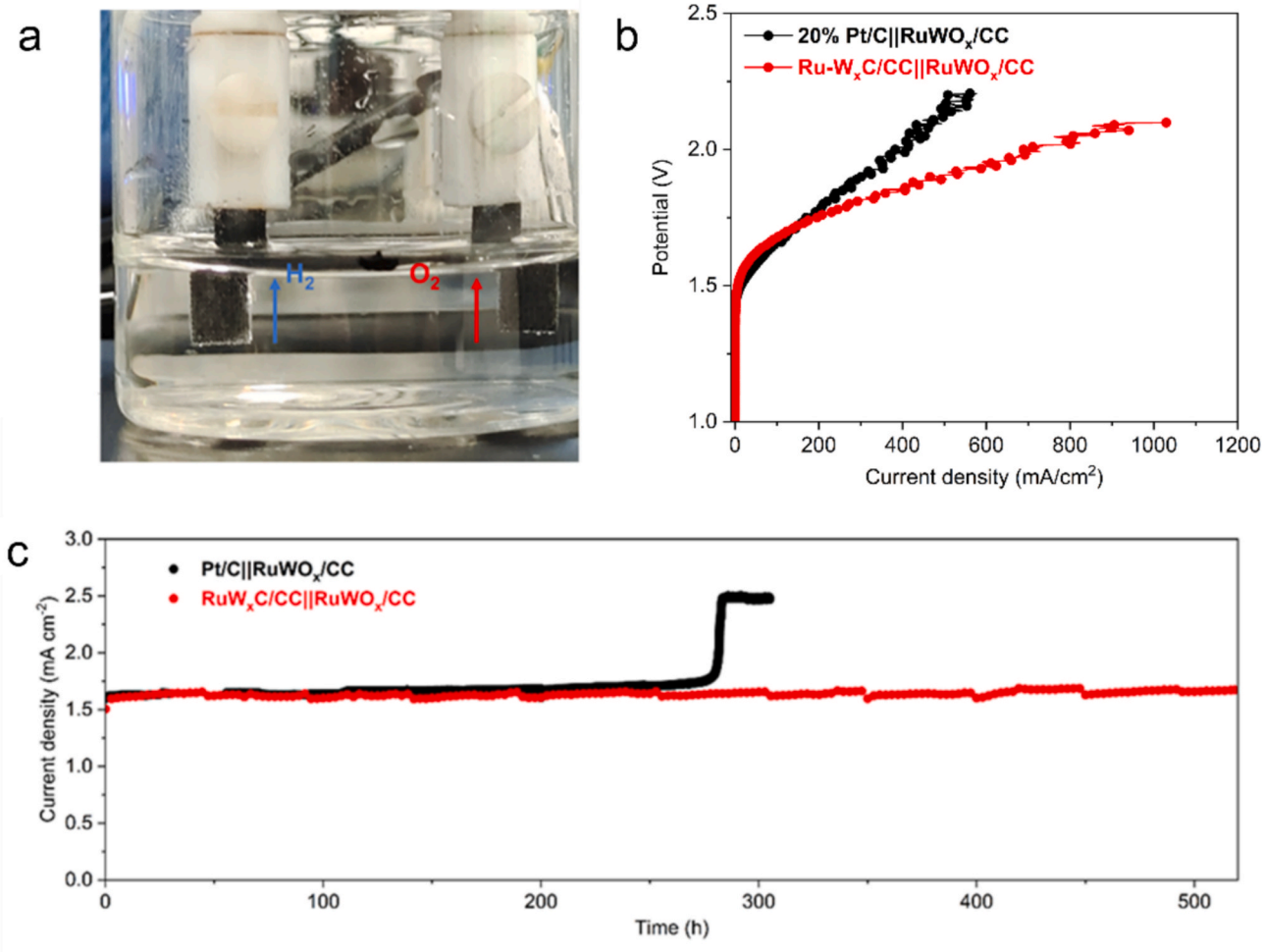

Fig. 5. a) Laboratory test diagram of overall water splitting in double electrode system. b) LSV comparison diagram of Ru-W_xC/CC || $RuWO_x$/CC and Pt/C || $RuWO_x$/CC. c) Stability test diagram of Ru-W_xC/CC || $RuWO_x$/CC at 10 mA cm^{-2}.

verified by density functional theory (DFT) [60]. To simulate the corresponding HER activity, the HER mechanism in acid consisting of the following three steps was considered, where the asterisk (*) indicated a certain surface species or an empty site [61–64]:

1) Volmer reaction: $H^+ + M + e^- - MH^*$
2) Heyrovsky reaction: $MH^* + H^+ + e^- - M + H_2$
3) Tafel reaction: $2MH^* - 2\,M + H_2$

The HER mechanism includes the Volmer-Heyrovsky or Volmer-Tafel pathway. Both pathways are involved in the formation of H*, and ΔG_{H^*} is an important index for predicting the activity of HER catalysts. This index is related to the electronic structure and surface chemistry of the catalysts. For an ideal catalytic site for the HER, the ΔG_{H^*} should approach to zero. Based on the TEM results, we constructed three catalyst models of Ru (002), two-phase heterostructure WC (100)/W_2C (102) and Ru (002)-WC (100)/W_2C (102), respectively (Figs. S25-27, Fig. 6a). To explore the optimized electronic structure of Ru around heterointerface, electron density difference at the interface region was plotted in Fig. 6b. It was found that the obvious electron accumulation and charge transfer at the heterostructure interface. HER activity was improved by regulating the electronic structure and optimizing binding energy through the heterostructure interface effect. The Bader charge diagram of WC (100)/W_2C (102) was shown in Fig. S28, and obvious electron accumulation and migration could also be found at the interface of the two-phase heterostructure. The charge transfer quantities of Ru, WC, and W_2C in Ru-W_xC/CC and W_xC/CC were shown in Table S2. The Bader charge value of Ru (002) was positive, indicating that there was an outflow of charge. Compared with W_xC/CC, the decrease of Bader charge value of WC (100) in Ru-W_xC/CC indicated that a large amount of charge transferred from W_2C to WC. These results were consistent with the XPS results. Ru NPs in Ru-W_xC/CC (−0.35 |e|) exhibited a charge close to the metallic state in Fig. 6c. According to the partial density of states (PDOS) plots in Fig. 6d. The d-band center value of Ru-WC/W_2C (Ru) was −2.94 eV. It was 0.03 eV lower than that of Ru (Ru), which indicated that the electron coupling between Ru and W atoms reduced the charge transfer resistance. According to the d-band theory, the downshift of the d-band center signified that the adsorption between Ru and reaction intermediates was weakened, which promotes the process of desorption. Ru-WC/W_2C (Ru) had a higher electron density near the fermi level, which facilitated the adsorption of H intermediates. Similarly, a similar conclusion could be obtained from the change of d-band center value at the W site. As a result, the adsorption/desorption of hydrogen intermediates was optimized. As revealed by Tafel slope results, the HER process of Ru-W_xC/CC in acidic environments followed a Volmer-Heyrovsky pathway, in which the reaction involved H_2O adsorption, H_2O dissociation, the formation of H* intermediates and H_2. The dissociation energy barrier diagram of water was shown in Fig. 6e.

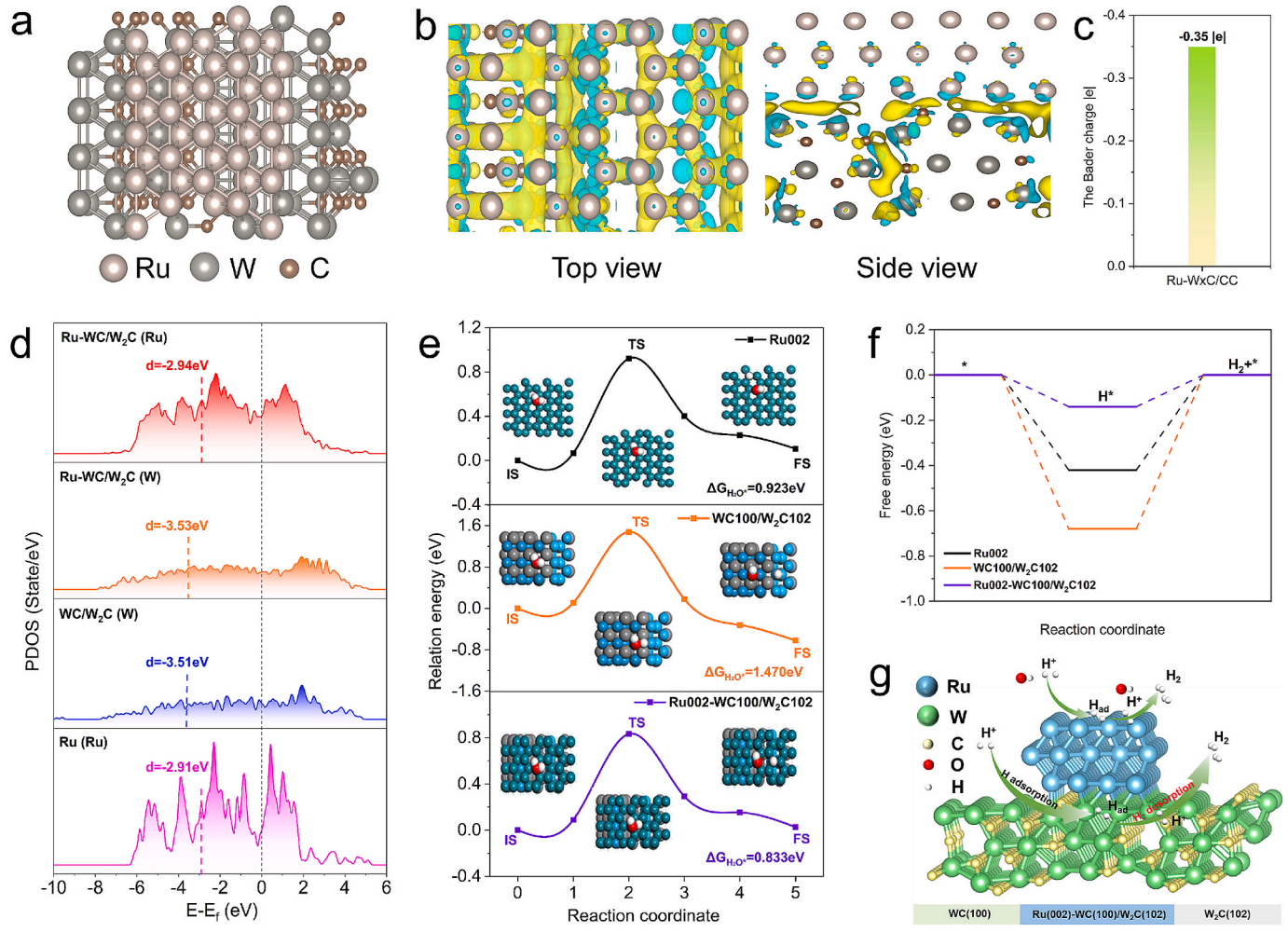

Fig. 6. a) Ru (002)-WC (100)/W_2C (102) calculation model diagram. b) Differential charge density of Ru-W_xC/CC. c) Bader charge analysis of Ru-W_xC/CC. d) The PDOS plots of Ru-W_xC/CC (Ru), Ru-W_xC/CC (W), W_xC/CC (W) and Ru (Ru). e) Dissociation energy barrier diagram of water and f) Hydrogen adsorption energy barrier diagram on Ru-W_xC/CC, W_xC/CC and Ru. g) Schematic illustration of heterointerface synergy between Ru, WC and W_2C for enhanced HER under few proton conditions.

The ΔG_{H2O^*} of Ru-WC/W_2C was 0.833 eV lower than Ru (ΔG_{H2O^*} = 0.923 eV) and WC/W_2C (ΔG_{H2O^*} = 1.47 eV), indicating that water was more easily dissociated in Ru-WC/W_2C. As shown in Fig. 6f, Ru-WC/W_2C had a lower hydrogen adsorption energy barrier ($\Delta G_{H^*} = -0.14$ eV), which was closer to zero than Ru ($\Delta G_{H^*} = -0.42$ eV) and WC/W_2C ($\Delta G_{H^*} = -0.68$ eV). This indicated that the introduction of Ru and more heterostructure interface could effectively promote the adsorption/desorption of hydrogen intermediates, thereby improving HER activity. This was consistent with the results of PDOS.

The elevated HER activity and stability of Ru-WC/W_2C in acidic media are related to the following aspects: Primarily, the strong electron coupling occurs at the Ru/W_xC and WC/W_2C two-phase heterostructure, which optimizes the electronic structure of Ru and W active sites, reduces the energy barrier of the reaction process and accelerates HER kinetics. This enhances the catalytic ability of the active site which facilitates the process of hydrogen desorption and water dissociation in acidic media. Fig. 6g showed two hydrogen evolution pathways. The H generated by hydrolysis is directly adsorbed on Ru interface or adsorbed at the three-phase heterogeneous interface to generate H*, then the H* combines with H ion derived from another H_2O molecule to form H_2. Furthermore, the uniform distribution of Ru-WC/W_2C NPs on the carbon carrier is not only conducive to the exposure of the active site and the acceleration of electron transfer but also conducive to the mass transfer of gas products, allowing for rapid separation of bubbles formed by high current density [51]. Thus, the high activity of the catalyst in acidic media and the highly durable HER performance in long-term operation are guaranteed.

4. Conclusion

In summary, Ru-W_xC/CC heterostructure is successfully developed by the ultrafast flash joule heating route. Ru NPs are uniformly dispersed on the heterointerface of WC/W_2C. DFT calculations demonstrate that the electronic interaction between Ru and W_xC optimizes the adsorption/desorption of H intermediates and the dissociation of H_2O. Their synergistic effect yields excellent activity for HER in acidic media, only exhibiting a low overpotential of 31 mV at 10 mA/cm^2, and 288 mV at 1 A/cm^2. The catalyst delivers a remarkable durability at least 500 h (at 10 mA cm^{-2}) for overall water splitting. This work not only provides a fast and efficient alternative for the synthesis of catalysts with excellent activity and stability but also provides guidance recommendations for the continued exploration of designing efficient electrocatalysts.

CRediT authorship contribution statement

Yongkang Liu: Methodology, Investigation, Formal analysis, Data curation. **Fulai Qi:** Writing – review & editing, Supervision, Investigation, Funding acquisition, Conceptualization. **Xinqiang Wang:** Investigation, Funding acquisition. **Qian Zhang:** Formal analysis, Data curation. **Yanxia Liu:** Methodology, Funding acquisition. **Yong Gao:** Software, Formal analysis. **Ke Wang:** Methodology, Formal analysis. **Wengang Cui:** Software, Methodology. **Fan Gao:** Methodology, Formal analysis. **Zhenglong Li:** Software, Formal analysis. **Yaxiong Yang:** Writing – review & editing, Formal analysis. **Lixian Sun:** Writing – review & editing, Supervision, Funding acquisition. **Jian Chen:** Writing – review & editing, Supervision, Funding acquisition. **Hongge Pan:** Writing – review & editing, Supervision, Funding acquisition, Conceptualization.

Declaration of competing interest

The authors declare that they have no known competing financial interests or personal relationships that could have appeared to influence the work reported in this paper.

Acknowledgements

The research was supported by the National Natural Science Foundation of China (Nos. 52301287 and 52201275), the Scientific Research Program Funded by Education Department of Shaanxi Provincial Government (No. 23JK0490), the Natural Science Foundation of Shaanxi Province (No. 2023-JC-QN-0470) the Major Special Project of the Integration of Two Chains for the Qin Chuangyuan Construction (No. 23LLRHZDZX0017), and the Foundation of Guangxi Key Laboratory of Information Materials (No. 221005-K).

Appendix A. Supplementary data

Supplementary data to this article can be found online at https://doi.org/10.1016/j.apsusc.2025.163015.

Data availability

Data will be made available on request.

References

[1] Z. Xu, Z. Wu, Scalable production of high-performance electrocatalysts for electrochemical water splitting at large current densities, eScience (2024) 2667, https://doi.org/10.1016/j.esci.2024.100334.
[2] L. Quan, H. Jiang, G. Mei, Y. Sun, B. You, Bifunctional electrocatalysts for overall and hybrid water splitting, Chem. Rev. 124 (2024) 3694–3812, https://doi.org/10.1021/acs.chemrev.3c00332.
[3] D. Wang, Q. Li, C. Han, Z. Xing, X. Yang, Single-atom ruthenium-based catalyst for enhanced hydrogen evolution, Appl. Catal. B: Environ. 249 (2019) 91–97, https://doi.org/10.1016/j.apcatb.2019.02.059.
[4] Z. Zhao, J. Sun, X. Li, S. Qin, C. Li, Z. Zhang, Z. Li, X. Meng, Engineering active and robust alloy-based electrocatalyst by rapid Joule-heating toward ampere-level hydrogen evolution, Nat. Commun. 15 (2024) 7475, https://doi.org/10.1038/s41467-024-51976-5.
[5] F. Guo, T.J. Macdonald, A.J. Sobrido, L. Liu, J. Feng, G. He, Recent advances in Ultralow-Pt-Loading electrocatalysts for the efficient hydrogen evolution, Adv. Sci. 10 (2023) 2301098, https://doi.org/10.1002/advs.202301098.
[6] H. Li, J. Guo, Z. Li, J. Wang, Research progress of hydrogen production technology and related catalysts by electrolysis of water, Molecules 28 (2023) 5010, https://doi.org/10.3390/molecules28135010.
[7] F. Xiao, M. Shao, Electrocatalyst and electrode design strategies for durable proton exchange membrane fuel cells, Matter 7 (2024) 351–377, https://doi.org/10.1016/j.matt.2023.11.009.
[8] Y. Lin, Y. Dong, X. Wang, L. Chen, Electrocatalysts for the oxygen evolution reaction in acidic media, Adv. Mater. 35 (2023) 2210565, https://doi.org/10.1002/adma.20221056.
[9] Z. Li, X. Liu, Q. Yu, X. Qu, J. Wan, Z. Xiao, J. Chi, L. Wang, Recent advances in design of hydrogen evolution reaction electrocatalysts at high current density: a review, Chin. J. Catal. 63 (2024) 33–60, https://doi.org/10.1016/S1872-2067 (24)60076-8.
[10] J. Gao, H. Tao, B. Liu, Progress of nonprecious-metal-based electrocatalysts for oxygen evolution in acidic media, Adv. Mater. 33 (2021) 2003786, https://doi.org/10.1002/adma.202003786.
[11] J. Ni, Z. Shi, Y. Wang, J. Yang, H. Wu, P. Wang, M. Xiao, C. Liu, W. Xing, Development of noble metal-free electrocatalysts towards acidic water oxidation: from fundamental understanding to state-of-the-art catalysts, eScience 5 (2) (2025) 2667, https://doi.org/10.1016/j.esci.2024.100295.
[12] C. Li, C. Yuan, X. Huang, H. Zhao, F. Wu, L. Xin, X. Zhang, S. Ye, Y. Chen, Tailoring the electron redistribution of RuO_2 by constructing a Ru-O-La asymmetric configuration for efficient acidic oxygen evolution, eScience 5 (1) (2025) 2667, https://doi.org/10.1016/j.esci.2024.100307.
[13] X. Zheng, J. Yang, X. Xu, S. Dou, W. Sun, D. Wang, G. Wang, Deciphering cationic and anionic overoxidation: key insights into the intrinsic structural degradation of catalysts, Adv. Energy Mater. 14 (2024) 2401227, https://doi.org/10.1002/aenm.202401227.
[14] L. Tao, F. Lv, D. Wang, H. Luo, F. Lin, H. Gong, H. Mi, S. Wang, Q. Zhang, L. Gu, M. Luo, S. Guo, Mass-efficient catalyst layer of hierarchical sub-nanosheets on nanowire for practical proton exchange membrane electrolyzer, Joule 8 (2024) 2542–4351, https://doi.org/10.1016/j.joule.2024.01.002.
[15] G. Gao, Z. Sun, X. Chen, G. Zhu, B. Sun, Y. Yamauchi, S. Liu, Recent advances in Ru/Ir-based electrocatalysts for acidic oxygen evolution reaction, Appl. Catal. B: Environ. 343 (2024) 123584, https://doi.org/10.1016/j.apcatb.2023.123584.
[16] H. Gao, Y. Jiang, R. Chen, C. Dong, Y. Huang, M. Ma, Z. Shi, J. Liu, Z. Zhang, M. Qiu, T. Wu, J. Wang, Y. Jiang, J. Chen, X. An, Y. He, S. Wang, Alloyed Pt Single-Atom catalysts for durable PEM water electrolyzer, Adv. Funct. Mater. 33 (2023) 2214795, https://doi.org/10.1002/adfm.202214795.
[17] W. Gou, Y. Wang, M. Zhang, XI. Tan, Y. Ma, Y. Qu, A review on fundamentals for designing stable ruthenium-based catalysts for the hydrogen and oxygen evolution

reactions, Chin. J. Catal. 60 (2024) 68–106, https://doi.org/10.1016/S1872-2067(24)60013-6.
[18] A. Al-Salihy, C. Liang, A. Salah, A.B. Al-Odayni, Z. Lu, M. Chen, Q. Liu, P. Xu, Ultralow Ru-doped $NiMoO_4$@$Ni_3(PO_4)_2$ core-shell nanostructures for improved overall water splitting, Chin. J. Catal. 60 (2024) 360–375, https://doi.org/10.1016/S1872-2067 (24) 60038-0.
[19] B. Zhang, J. Wang, G. Liu, C. Weiss, D. Liu, Y. Chen, L. Xia, P. Zhou, M. Gao, Y. Liu, J. Chen, Y. Yan, M. Shao, H. Pan, W. Sun, A strongly coupled Ru-CrO_x cluster–cluster heterostructure for efficient alkaline hydrogen electrocatalysis, Nat. Catal. 7 (2024) 441–451, https://doi.org/10.1038/s41929-024-01126-3.
[20] A. Salah, L. Zhang, H. Tan, F. Yu, Z. Lang, N. Al-Ansi, Y. Li, Advanced Ru/Ni/WC@NPC Multi-Interfacial electrocatalyst for efficient sustainable hydrogen and Chlor-Alkali Co-Production, Adv. Energy Mater. 12 (2022) 2200332, https://doi.org/10.1002/aenm.202200332.
[21] Q. Wang, M. Ming, S. Niu, Y. Zhang, G. Fan, J. Hu, Scalable Solid-State synthesis of highly dispersed uncapped metal (Rh, Ru, Ir) nanoparticles for efficient hydrogen evolution, Adv. Energy Mater. 8 (2018) 1801698, https://doi.org/10.1002/aenm.201801698.
[22] D.H. Kweon, M.S. Okyay, S.J. Kim, J.P. Jeon, H.J. Noh, N. Park, J. Mahmood, J. B. Baek, Ruthenium anchored on carbon nanotube electrocatalyst for hydrogen production with enhanced Faradaic efficiency, Nat. Commun. 11 (2020) 1278, https://doi.org/10.1038/s41467-020-15069-3.
[23] Z. Bao, J. Wang, Z. Zhang, H. Xing, Q. Yang, Y. Yang, H. Wu, R. Krishna, W. Zhou, B. Chen, Q. Ren, Molecular sieving of ethane from ethylene through the molecular cross-section size differentiation in Gallate-based Metal–Organic frameworks, Angew. Chem. Int. Ed. 57 (2018) 16020–16025, https://doi.org/10.1002/anie.201808716.
[24] Z. Yu, C. Si, F.J. Escobar-Bedia, A.P. LaGrow, J. Xu, M.J. Sabater, I. Amorim, A. Araujo, P.S. Sousa, L. Meng, J.L. Faria, P. Concepcion, B. Li, L. Liu, Bifunctional atomically dispersed ruthenium electrocatalysts for efficient bipolar membrane water electrolysis, Inorg. Chem. Front. 9 (2022) 4142–4150, https://doi.org/10.1039/D2QI00892K.
[25] L. Xing, H. Gao, G. Hai, Z. Tao, J. Zhao, D. Jia, X. Chen, M. Han, S. Hong, L. Zheng, X. Huang, W. Dong, G. Wang, X. Shu, Atomically dispersed ruthenium sites on whisker-like secondary microstructure of porous carbon host toward highly efficient hydrogen evolution, J. Mater. Chem. A 8 (2020) 3203–3210, https://doi.org/10.1039/C9TA11280D.
[26] H. Zhang, N. Li, S. Gao, A. Chen, Q. Qian, Q. Kong, B. Xia, G. Hu, Quenching-induced atom-stepped bimetallic sulfide heterointerface catalysts for industrial hydrogen generation, eScience 5 (2) (2025) 2667, https://doi.org/10.1016/j.esci.2024.100311.
[27] Y. Zhang, Y. Lin, T. Duan, L. Song, Interfacial engineering of heterogeneous catalysts for electrocatalysis, Mater. Today 48 (2021) 115–134, https://doi.org/10.1016/j.mattod.2021.02.004.
[28] R. Yao, H. Zhao, F. Yu, W. Zhang, G. Yan, Y. Li, Y. Wang, H. Tan, Y. Li, Interfacial engineering of Ni/WC heterostructure electrocatalyst for highly efficient hydrogen evolution reaction in all pH electrolyte, J. Alloys Compd. 972 (2024) 172827, https://doi.org/10.1016/j.jallcom.2023.172827.
[29] J. Ren, L. Chen, H. Wang, W. Tian, X. Zhang, T. Ma, Z. Zhou, Z. Yuan, Inducing electronic asymmetricity on Ru clusters to boost key reaction steps in basic hydrogen evolution, Appl. Catal. B: Environ. 327 (2023) 122466, https://doi.org/10.1016/j.apcatb.2023.122466.
[30] S. Li, B. Chen, Y. Wang, Oxygen-evolving catalytic atoms on metal carbides, Nat. Mater. 20 (2021) 1240–1247, https://doi.org/10.1038/s41563-021-01006-2.
[31] Y. Cheng, H. Wang, T. Qian, C. Yan, Interfacial engineering of carbon-based materials for efficient electrocatalysis: recent advances and future, EnergyChem 100074 (2022) 2589–7780, https://doi.org/10.1016/j.enchem.2022.100074.
[32] Y. Wang, J. Chen, L. Gong, J. Tang, X. Wang, H. Guo, X. Zhou, P-doped W_2C nanoparticles for hydrogen evolution reaction powered by a wind-driven triboelectric nanogenerator, Nano Energy 121 (2024) 109242, https://doi.org/10.1016/j.nanoen.2023.109242.
[33] T. Chao, W. Xie, Y. Hu, G. Yu, T. Zhao, C. Chen, Z. Zhang, X. Hong, H. Jin, D. Wang, W. Chen, X. Li, P. Hu, Y. Li, Reversible hydrogen spillover at the atomic interface for efficient alkaline hydrogen evolution, Energy Environ. Sci. 1397 (2024) 1754–5692, https://doi.org/10.1039/D3EE02760K.
[34] S. Wang, L. Wang, W. He, D. Liu, H. Wang, W. Yu, D. Yin, X. Dong, Pt and Mo_2C nanoparticles embedded in hollow carbon nanofibers as an effective electrocatalyst for hydrogen evolution reaction in acidic and alkaline electrolytes, J. Alloys Compd. 1005 (2024) 176019, https://doi.org/10.1016/j.jallcom.2024.176019.
[35] J. Liu, P. Guo, D. Liu, X. Yan, X. Tu, H. Pan, R. Wu, Activating TiO_2 through the phase transition-mediated hydrogen spillover to outperform Pt for electrocatalytic pH-universal hydrogen evolution, Small 20 (2024) 2400783, https://doi.org/10.1002/smll.202400783.
[36] X. Teng, D. Si, L. Chen, J. Shi, Synergetic catalytic effects by strong metal–support interaction for efficient electrocatalysis, eScience 4 (6) (2024) 2667-1417, https://doi.org/10.1016/j.esci.2024.100272.
[37] Y. Li, Z. Dou, Y. Pan, H. Zhao, L. Yao, Q. Wang, C. Zhang, Z. Yue, Z. Zou, Q. Cheng, H. Yang, Crystalline phase engineering to modulate the interfacial interaction of the ruthenium/molybdenum carbide for acidic hydrogen evolution, Nano Lett. 24 (2024) 5705–5713, https://doi.org/10.1021/acs.nanolett.4c00495.
[38] J. Jiang, S. Liu, Z. Li, M.G. Kim, H. Jang, X. Liu, L. Hou, Lattice-Matched Ru/W_2C heterointerfaces with reversible hydrogen spillover for efficient alkaline hydrogen evolution, Adv. Energy Mater. (2024) 2405546, https://doi.org/10.1002/aenm.202405546.
[39] X. Zheng, X. Gao, R. Vilá, Y. Jiang, J. Wang, R. Xu, R. Zhang, X. Xiao, P. Zhang, L. Greenburg, Y. Yang, H. Xin, X. Zheng, Y. Cui, Hydrogen-substituted graphdiyne-assisted ultrafast sparking synthesis of metastable nanomaterials, Nat. Nanotechnol. 18 (2023) 153–159, https://doi.org/10.1038/s41565-022-01272-4.
[40] A. Abdelhafiz, B. Wang, A.R. Harutyunyan, J. Li, Carbothermal shock synthesis of high entropy oxide catalysts: dynamic structural and chemical reconstruction boosting the catalytic activity and stability toward oxygen evolution reaction, Adv. Energy Mater. 12 (2022) 2200742, https://doi.org/10.1002/aenm.202200742.
[41] H. Zhang, S. Qi, K. Zhu, H. Wang, G. Zhang, W. Ma, X. Zong, Ultrafast synthesis of Mo_2C-based catalyst by joule heating towards electrocatalytic hydrogen evolution reaction, Symmetry 15 (2023) 801, https://doi.org/10.3390/sym15040801.
[42] A. Zhou, W. Guo, Y. Wang, J. Zhang, The rapid preparation of efficient MoFeCo-based bifunctional electrocatalysts via joule heating for overall water splitting, J. Electrochem. 28 (2022) 2214007, https://doi.org/10.13208/j.electrochem.2214007.
[43] C. Wang, P. Li, L. Zong, K. Fan, F. Lu, Z. Wang, L. Wang, High-temperature shock enabled synthesis of ultrafine Ru nanoparticles anchoring onto tungsten carbide with strong metal-support interaction for ampere-level current density hydrogen evolution, J. Alloys Compd. 967 (2023) 171667, https://doi.org/10.1016/j.jallcom.2023.171667.
[44] J. Lei, X. Fan, T. Liu, P. Xu, Q. Hou, K. Li, R. Yuan, M. Zheng, Q. Dong, J. Chen, Single-dispersed polyoxometalate clusters embedded on multilayer graphene as a bifunctional electrocatalyst for efficient Li-S batteries, Nat. Commun. 13 (2022) 202, https://doi.org/10.1038/s41467-021-27866-5.
[45] P. Zheng, L. Wang, Q. Wang, J. Zhang, Enhanced capacitive deionization by rGO@PEI/MoS_2 nanocomposites with rich heterostructures, Sep. Purif. 295 (2022) 121156, https://doi.org/10.1016/j.seppur.2022.121156.
[46] I.V. Kozhevnikov, Heteropoly acids and related compounds as catalysts for fine chemical synthesis, Catal. Rev. 37 (1995) 311–352, https://doi.org/10.1080/01614949508007097.
[47] S. Piccinin, S. Fabris, Water oxidation by Ru-polyoxometalate catalysts: overpotential dependency on the number and charge of the metal centers, Inorganics 3 (2015) 374–387, https://doi.org/10.3390/inorganics3030374.
[48] X. Zhu, L. Xu, C. Cui, Q. Liu, H. Wang, Preparation and characterization of zirconium carbide nano powder by hydrothermal and carbothermal reduction methods, Ceram. Int. 50 (2024) 30151–30160, https://doi.org/10.1016/j.ceramint.2024.05.314.
[49] C. Li, Z. Wang, M. Liu, E. Wang, B. Wang, L. Xu, K. Jiang, S. Fan, Y. Sun, J. Li, K. Liu, Ultrafast self-heating synthesis of robust heterogeneous nanocarbides for high current density hydrogen evolution reaction, Nat. Commun. 13 (2022) 3338, https://doi.org/10.1038/s41467-022-31077-x.
[50] S. Sun, H. Jiang, Z. Chen, Q. Chen, M. Ma, L. Zhen, B. Song, C. Xu, Bifunctional WC-supported RuO_2 nanoparticles for robust water splitting in acidic media, Angew. Chem. Int. Ed. 61 (2022) e202202519, https://doi.org/10.1002/anie.202202519.
[51] L. Hong, D. Lan, X. Zheng, Y. Nan, Y. Hu, B. Yu, X. Guo, Synergistic effect of Ru nanoclusters on WC_{1-x} anchored on N-doped carbon nanosheets to promote highly efficient alkaline hydrogen evolution, Inorg. Chem. Front. 10 (2023) 137–147, https://doi.org/10.1039/D2QI01923J.
[52] T. Chao, W. Xie, Y. Hu, G. Yu, T. Chen, C. Zhang, Z. Hong, X. Jin, H. Wang, D. Chen, W. Li, X. Hu, P. Li, Reversible hydrogen spillover at the atomic interface for efficient alkaline hydrogen evolution, Energy Environ. Sci. 17 (2024) 1397–1406, https://doi.org/10.1039/D3EE02760K.
[53] J. Cai, W. Zhang, Y. Liu, R. Shen, X. Xie, W. Tian, X. Zhang, J. Ding, Y. Liu, B. Li, Interfacial synergistic effect of Ru nanoparticles embedded onto amorphous/crystalline WO_3 nanorods on boosting the pH-universal hydrogen evolution reaction, Appl. Catal. B: Environ. 343 (2024) 123502, https://doi.org/10.1016/j.apcatb.2023.123502.
[54] L. Wang, Z. Xu, C. Kuo, J. Peng, F. Hu, L. Li, H. Chen, J. Wang, S. Peng, Stabilizing Low-Valence single atoms by constructing metalloid tungsten carbide supports for efficient hydrogen oxidation and evolution, Angew. Chem. Int. Edit. 62 (2023) e202311937, https://doi.org/10.1002/anie.202311937.
[55] S. Sun, F. Ma, H. Jiang, M. Chen, P. Xu, L. Zhen, B. Song, C. Xu, C. Xu, Encapsulating dual-phase WC-W_2C nanoparticles into hollow carbon dodecahedrons for all-pH electrocatalytic hydrogen evolution, Chem. Eng. J. 462 (2023) 142132, https://doi.org/10.1016/j.cej.2023.142132.
[56] M. Rafique, Q. Fu, J. Han, R. Wang, T. Yao, X. Wang, B. Song, Tungsten carbide-based materials for electrocatalytic water splitting: a review, ChemElectroChem 11 (2024) e202300722, https://doi.org/10.1002/celc.202300722.
[57] H. Du, Z. Du, T. Wang, S. He, K. Yang, K. Wang, L. Xie, W. Ai, W. Huang, Interface engineering of tungsten carbide/phosphide heterostructures anchored on N, P-codoped carbon for high-efficiency hydrogen evolution reaction, Sci. China Mater. 65 (2022) 967–973, https://doi.org/10.1007/s40843-021-1834-4.
[58] C. Cai, K. Liu, Y. Zhu, P. Li, Q. Wang, B. Liu, S. Chen, H. Li, L. Zhu, H. Li, J. Fu, Y. Chen, E. Pensa, J. Hu, Y. Lu, T. Chan, E. Cortés, M. Liu, Optimizing hydrogen binding on Ru sites with RuCo Alloy nanosheets for efficient alkaline hydrogen evolution, Angew. Chem. Int. Ed. 61 (2022) e202113664, https://doi.org/10.1002/anie.202113664.
[59] H. Chen, J. Yu, L. Liu, R. Gao, Z. Gao, Y. Yang, Z. Chen, S. Zhan, X. Liu, X. Zhang, H. Dong, L. Wu, L. Wang, Modulating Pt-N/O bonds on Co-doped WO_3 for acid electrocatalytic hydrogen evolution with over 2000 h operation, Adv. Energy Mater. 14 (2024) 2303635, https://doi.org/10.1002/aenm.202303635.
[60] C. Zhao, J. Liu, B. Li, D. Ren, X. Chen, J. Yu, Q. Zhang, Multiscale construction of bifunctional electrocatalysts for Long-Lifespan rechargeable Zinc-Air batteries, Adv. Funct. Mater. 30 (2020) 2003619, https://doi.org/10.1002/adfm.202003619.
[61] G. Gao, X. Chen, L. Han, G. Zhu, J. Jia, A. Cabot, Z. Sun, Advances in MOFs and their derivatives for non-noble metal electrocatalysts in water splitting, Coord. Chem. Rev. 503 (2024) 215639, https://doi.org/10.1016/j.ccr.2023.215639.

[62] A. Song, S. Song, M. Duanmu, H. Tian, H. Liu, X. Qin, G. Shao, G. Wang, Recent progress of Non-Noble metallic heterostructures for the electrocatalytic hydrogen evolution, Small Sci. 3 (2023) 2300036, https://doi.org/10.1002/smsc.202300036.

[63] Y. Shi, B. Zhang, Recent advances in transition metal phosphide nanomaterials: synthesis and applications in hydrogen evolution reaction, Chem. Soc. Rev. 45 (2016) 1529, https://doi.org/10.1039/C6CS90013E.

[64] B. Wang, F. Yang, L. Feng, Recent advances in Co-based electrocatalysts for hydrogen evolution reaction, Small 19 (2023) 2302866, https://doi.org/10.1002/smll.202302866.